Iron fluoride with excellent cycle performance synthesized by solvothermal method as cathodes for lithium ion batteries

Jinli Tan, Li Liu*, Hai Hu, Zhenhua Yang, Haipeng Guo, Qiliang Wei, Xin Yi, Zichao Yan, Qian Zhou, Zhifeng Huang, Hongbo Shu, Xiukang Yang, Xianyou Wang*

School of Chemistry, Key Laboratory of Environmentally Friendly Chemistry and Applications of Ministry of Education, Xiangtan University, Xiangtan 411105, China

HIGHLIGHTS

- Iron fluoride with hollow prismatic/cylindric structure has been firstly obtained.
- The formation mechanism of prismatic/cylindric structure has been proposed.
- $FeF_3 \cdot 0.33H_2O$/C nanocomposites show an excellent performance.

ARTICLE INFO

ABSTRACT

Hollow prismatic/cylindric iron fluoride with a wall thickness of 0.1–0.5 μm and a length of 1–3 μm has been synthesized by a simple and mild solvothermal method. This compound with a mixed crystal structure of $FeF_3 \cdot 3H_2O$ and $FeF_3 \cdot 0.33H_2O$, has an initial discharge capacities of 106.7 mAh g^{-1} and a capacity retention of 60% after 100 cycles at the rate of 0.5C (1 C is 237 mA g^{-1}) in the voltage of 2.0 –4.5 V. To overcome the poor electronic conductivity of fluorides, the as-prepared iron fluoride has been ball-milled with 15 wt.% acetylene black (AB) and heat-treated to obtain $FeF_3 \cdot 0.33H_2O$/C nano-composites. The nanocomposites deliver discharge capacity of 160.2 mAh g^{-1} at the rate of 0.5C. Even at the high rate of 5 C, the initial discharge capacity is still as high as 137.5 mAh g^{-1}. The capacity retentions reach up to 85.0% and 75.7% after 100 cycles at 0.5 C and 5 C, respectively.

1. Introduction

The arrival of Li ion battery technology brings an innovation for portable electronic products. Vast researches have focused on the discovery and development of electrodes materials to meet the growing demand of high power devices such as electric vehicles (EVs) and hybrid electric vehicles (HEVs). Metal fluorides, owing to their ionic character, high operating voltages, high energy density and power, are developing as a promising alternative cathode materials for lithium ion batteries (LIBs) [1,2]. Among these, iron fluoride is of the great interest on account of low cost, high theoretical specific capacity (237 mAh g^{-1} for 1e^- transfer), high discharge voltage, and environmental friendliness. In spite of these advantages, wide band gap of Fe–F bonds is a fatal shortcoming for

iron fluoride that leads a poor electronic conductivity of materials, making the actual specific capacity far below the theoretical value and hindering its practical application [3]. Arial et al. [4] were the first to report FeF_3 as the cathode materials for LIBs, as would be expected, a limited reversible capacity of only 80 mAh g^{-1} was achieved in a discharge voltage region from 2.0 to 4.5 V.

Decreasing the size of grain and adding conductive materials are two kinds of effective methods to improve electrochemical performance of cathode materials. The fabrication of micro/nano-structured materials has attracted considerable attention for they can enlarge the contact area with the electrolyte, increase the surface reactivity and shorten both electronic and ionic pathways within particle [5,6]. There are a mass of reports on oxide systems as anode/cathode materials [7,8], most of them exhibit superior rate capability and cycling stability as anodes/cathode materials for LIBs owing to their prominent structure features. Li et al. [9] synthesized nanostructured $FeF_3 \cdot 0.33H_2O$ in the $BmimBF_4$ liquid medium, a significantly ameliorative capacity of 126 mAh g^{-1} can be achieved at

* Corresponding authors. Tel.: +86 731 58292206; fax: +86 731 58292477.
 E-mail addresses: liulili1203@126.com (L. Liu), wxianyou@yahoo.com (X. Wang).

a current density of 71 mA g^{-1}, but only 30 cycles were lasted. Chu et al. [10] prepared porous FeF$_3$ nanospheres via introducing FeF$_3$ aqueous solution into ethanol. The porous nanospheres show good cycling performance and rate capability. A reversible discharge capacity of 144 mAh g^{-1} can be retained after 50 cycles at the current density of 50 mA g^{-1}. However, it did not say more about the performance after 50 cycles. So it is not very encouraging just via reducing the grains size to solve the poor conductivity of fluorides. To overcome this issue, several approaches have been reported such as metal doping [11], activated carbon coating [12], in situ signal-wall carbon nanotubes or graphene introduction [13–16]. Zhang et al. [17] synthesized three-dimensionally ordered macroporous (3DOM) FeF$_3$/poly(3, 4-ethylenedioxythiophene) (PEDOT) composite using polystyrene (PS) colloidal crystals as hard template through in situ polymerization method. The hybrid nanostructures with a high reversible discharge capacity reach up to 210 mAh g^{-1} at a current density of 20 mA g^{-1} and a good rate capability of 120 mAh g^{-1} at a high current density of 1 A g^{-1} with the scope of 2.0–4.5 V at room temperature. Li et al. prepared [13] signal-wall carbon nanotubes (SWNTs)/FeF$_3$·0.33H$_2$O in the BmimBF$_4$ medium via liquid-phase method, this composite materials exhibit a remarkable capacity performance, and deliver discharge capacity of 220 mAh g^{-1} at 0.1 C. Namely, the introduction of conductive polymer or carbon can greatly improve the electrochemical performance of iron fluoride. However, it is not worthwhile from the aspect of cost. BmimBF$_4$ ionic liquid and SWNTs are very expensive, and it is hard to form well disentangled and dispersed SWNTs. Additional, when relating to polymer, it is inevitable that harmful organic solvents usage, cumbersome synthesis process and post-processing. Therefore, these methods are not suitable for industrial production.

Adding conductive carbon (such as AB) to fluoride materials by ball-milling is a simple and effective method. Active materials and AB can mix together heterogeneously and a conductive network can be formed between them after ball-milling, then an increase of the electronic conductivity can be obtained. Amatucci and his co-worker [18] prepared carbon metal fluoride nanocomposites (CMFNCs) by ball-milling FeF$_3$ with conductive carbon. The synthetic CMFNCs showed an initial discharge capacity of about 170 mAh g^{-1} at a current density of 7.58 mA g^{-1} in the range of 2.0–4.5 V. In our previous studies [11,19], either Co-doping or the comparison among FeF$_3$·3H$_2$O, FeF$_3$·0.33H$_2$O and FeF$_3$, the electrochemical properties of iron fluorides can be further improved through ball-milling with AB. The ball-milled materials showed a prominent discharge capacity and cycle stability even at the high rates on account of nanosized crystals formed through ball-milling have a high total material volume on the surface in which contains a number of defects which can contribute substantially to enhance electronic and ionic activity [18], the conductive network formed between fluorides and AB also can increase the electronic conductivity of materials. Therefore, ball-milling metal fluoride with conductive materials is an effective way to improve electrochemical properties.

Besides, it is ideal to synthesize iron fluorides that possess optimal morphology by using appropriate chemical method. Solvothermal method is widely applied in preparing nano-materials, porous materials, and hollow materials in recent years [20,21]. It has a lot of advantages such as fast reaction kinetics, short processing times, high crystallinity and yield, homogeneous and narrow particle-size distributions. Most importance, it is cost effective, environmentally benign, and easily scale-able [22]. The materials obtained from this method usually show great developments in discharge/charge, cyclability, rate capability, and cheap synthesis in comparison with conventional methods.

In this work, hollow prismatic/cylindric iron fluorides compounds with a mixed crystal structure consisting of FeF$_3$·3H$_2$O and FeF$_3$·0.33H$_2$O have been synthesized by a time-dependent solvothermal method and their formation mechanism also have been researched. After ball-milling with AB and heating, FeF$_3$·0.33H$_2$O/C nanocomposites with even particle sizes can be obtained, which are found to exhibit superior cycling stability as cathode materials for LIBs.

2. Experiments section

2.1. Synthesis of materials

Firstly, 8.08 g Fe(NO$_3$)$_3$·9H$_2$O was dissolved in 50 mL ethanol. Then, Fe(NO$_3$)$_3$·ethanol was added to the mixed solution which consists of 20 mL HF aqueous solution (40 wt.%) and 0.05 g CTAB. When Fe(NO$_3$)$_3$·ethanol was added into CTAB/HF aqueous solution which had been ultrasonic-treated in the teflon wares, it will react immediately to form colorless FeF$_6^{3-}$ due to its high stability ($K_f = 10^{15.04}$). In aqueous-based solution, FeF$_6^{3-}$ readily converted to FeF$_3$·3H$_2$O [19]. Next, the sealed Teflon ware was put into a stainless steel autoclave, which was hold at 80 °C for 1 h, 2 h and 4 h, respectively, followed by cooling at the room temperature to obtain pink precipitates. The precipitates were washed by ethanol and stirred at 80 °C to remove the un-reacted HF and water in the oil bath and the residue was dried at 180 °C for 12 h at oven and cooled down naturally. To distinguish the products preferably, three kinds of compounds have been named as F1, F2, and F4 which correspond to reaction for 1 h, 2 h, and 4 h, respectively. Then F2 was ball-milled with AB at 320 rpm for 3 h (the weight ratio of iron fluoride: AB is 85:15) and dried at 180 °C for 6 h to form iron fluoride/C nanocomposites, which were named as F2/C.

2.2. Characterizations and measurements

The structures of samples were characterized by X-ray diffraction on a Rigaku D/MAX-2500 powder diffractometer at 40 kV and 100 mA using a graphite monochromatic and Cu-Ka radiation ($k = 0.15418$ nm) operated with a scan rate of 4° min^{-1} in the 2θ range of 10°–80°.

The morphologies were investigated by using a JEOL JSM-6610LV scanning electron microscope (SEM). High-resolution transmission electron microscopy (HRTEM) and selected-area electron diffraction (SAED) measurements were carried out using a JEOL JEM-2100F transmission electron microscope (TEM) at an acceleration voltage of 200 kV.

The cathodes for testing cells were fabricated by mixing the cathode materials, carbon black, and polyvinylidene fluoride (PVDF) binder with a weight ratio of 80:10:10 in N-methyl pyrrolidinone, which were then pasted on aluminum foil followed by drying under vacuum at 110 °C for 24 h. The testing cells were assembled with the cathodes thus fabricated, metallic lithium anode, Celgard 2300 film separator, and 1 M LiPF$_6$ in 1:1 ethylene carbonate (EC)/dimethyl carbonate (DMC) electrolyte. The assembly of the cells was carried out in an argon-filled glove box, where water and oxygen concentration were kept less than 5 ppm. All the cells were allowed to age for 12 h before testing. Charge–discharge measurements were performed at room temperature under different rates in a voltage range of 2.0–4.5 V on the Neware battery test system.

Cyclic voltammetry (CV) tests and electrochemical impedance spectroscopy (EIS) were performed on a Zahner Zennium electrochemical workstation. CV tests were carried out at a constant scanning rate of 1 mV s^{-1} on the potential interval 2.0–4.5 V (vs. Li$^+$/Li). The ac perturbation signal was ±5 mV and the frequency range was from 100 mHz to 100 KHz.

The galvanostatic intermittent titration technique (GITT) was performed at room temperature under a small current flux of 0.1 C

(1 C is 237 mA g^{-1}) and a long time interval of 60 min in a voltage range of 2.0–4.5 V on the Neware battery test system.

3. Results and discussion

The XRD patterns of samples are shown in Fig. 1a. It can see clearly from the patterns of Fig. 1a that the diffraction peaks of F1, F2 and F4 match up with the tetragonal $FeF_3 \cdot 3H_2O$ (JCPD card no. 32-0464, space group P4/n) and orthorhombic $FeF_3 \cdot 0.33H_2O$ (JCPD card no. 76-1262, space group Cmcm). F1 and F2 show relatively intense peaks at $2\theta = 13.8°, 23.6°$ and $27.8°$ corresponding to (110), (002), and (220) diffraction peaks of $FeF_3 \cdot 0.33H_2O$. F4, however, appears relatively intense peaks at $16.0°, 25.6°$ and $36.3°$ in the XRD patterns corresponding to (110), (101) and (310) of tetragonal $FeF_3 \cdot 3H_2O$. The relative intensity of $FeF_3 \cdot 3H_2O$ and $FeF_3 \cdot 0.33H_2O$ in the XRD patterns gradually increases. The intensity of diffraction peaks increases with the increase of reaction time, indicating that the samples are further crystallized with the increase of reaction time. It is clear that the capacity retention is related to the crystallinity [23,24]. Good crystallinity implies an unhindered Li$^+$ diffusion in the lattice and the consequent low polarization and high capacity retention [23,24].

The cell structure and crystallographic views along the [001] direction of tetragonal $FeF_3 \cdot 3H_2O$ and orthorhombic $FeF_3 \cdot 0.33H_2O$ presented in Fig. 1b–e to describe the intercalation reaction of Li$^+$ in $FeF_3 \cdot nH_2O$ simply. Four Irregular Octahedral $Fe(F_4O_2)$ in $FeF_3 \cdot 3H_2O$ (Fig. 1b, c) are unconnected to each other along the direction of [001] to form a quadrangular cavity which may be able to accommodate Li$^+$ and brings a cell volume of ~240 Å^3. Hydrogen bonds between water molecules lying in the center of quadrangular cavity and adjacent ligands are relied on maintaining the structure stability. In the structure of $FeF_3 \cdot 0.33H_2O$ (Fig. 1d, e), six FeF_6 form a special huge hexagonal cavity via corner-sharing to resulting in much larger cell volumes (~710 Å^3). The trace amount of water
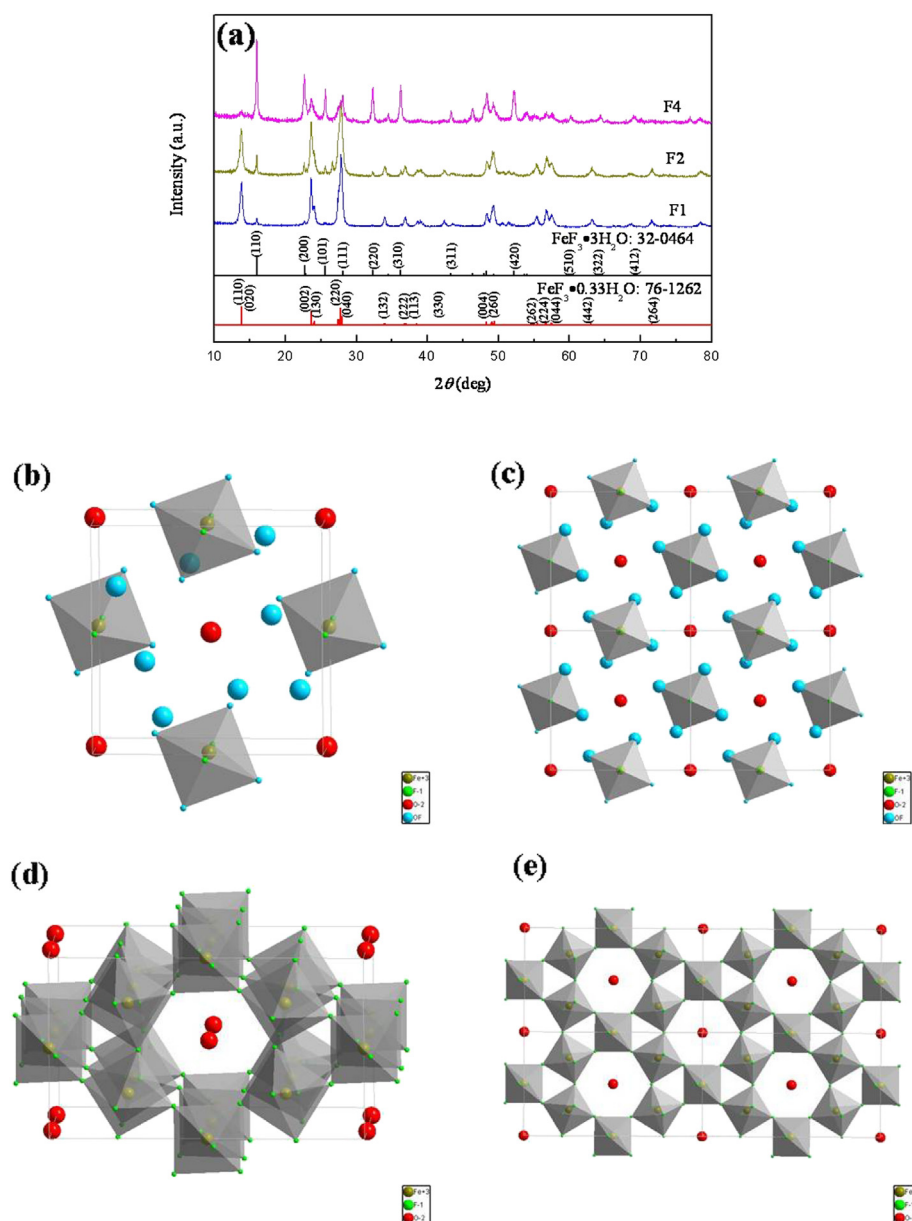

Fig. 1. XRD patterns of F1, F2 and F4 (a); Cell structures of tetragonal $FeF_3 \cdot 3H_2O$ (b), orthorhombic $FeF_3 \cdot 0.33H_2O$ (d); Projections of $FeF_3 \cdot 3H_2O$ (c), $FeF_3 \cdot 0.33H_2O$ (e) along the direction of [001].

containing in $FeF_3 \cdot 0.33H_2O$ exist stably in the huge hexagonal cavity and plays a part of structural stabilizer to stabilize the huge hexagonal cavity and avoid structure collapse during Li^+ insertion and extraction processes [19,25]. Therefore, these two kinds of iron fluorides can prove the space for accommodation and transport Li^+.

The morphology and particle size of F1, F2 and F4 collected by SEM are presented in Fig. 2. These images show that these three kinds of samples have totally distinct morphologies. F1 consists of some incomplete sheet prismatic and cylindric frameworks. Sheet particles are easily broken undergoing high temperature, in order to present original features of sheet grains preferably, the sheet grains of F1 without heat-treating at 180 °C show in the inset of Fig. 2a. The shorter side of F1 is about 1–2 μm, the longer side is about 2–4 μm and the wall thickness is about 0.1–0.5 μm (Fig. 2a, b). Fig. 2c, d exhibit the particles morphology of F2. There is an extremely peculiar morphology that a cavity consists in the center of the prismatic and cylindric particles. The lengths of side of F1 and F2 are similar, but the wall of F2 (∼0.5 μm) is much thicker than F1 and the polyhedron shape is much complete comparing with F1. The solid cubes come from the reaction for 4 h (Fig. 2e, f) that the shorter side is about 20–50 μm and the longer side is about 50–100 μm.

On the basis of all the above observations, a simple plausible mechanism was proposed addressing the template-free formation
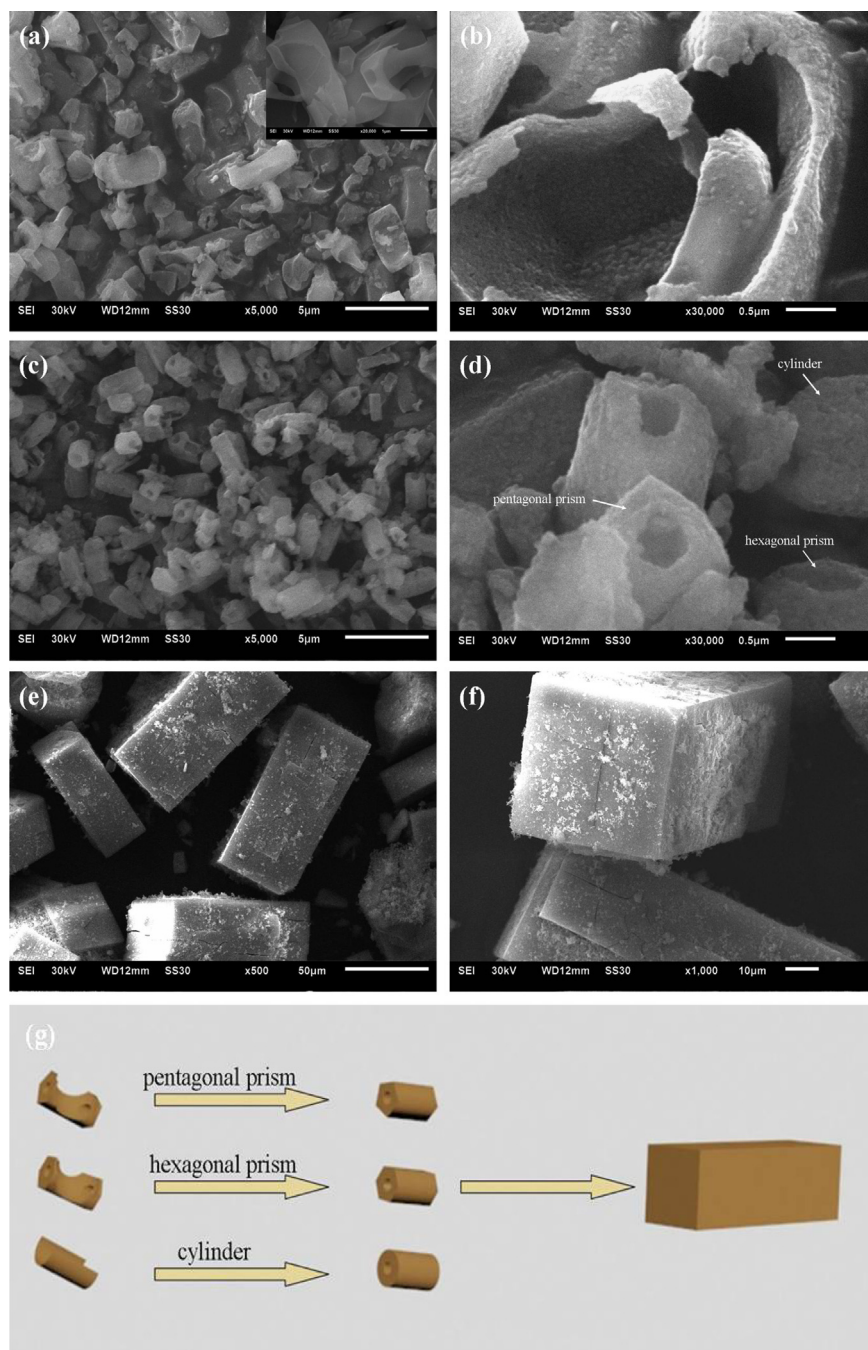

Fig. 2. SEM images of F1 (a, b) (inset: the sheet particles without heat-treating at 180 °C), F2 (c, d) and F4 (e, f). Schematic illustration of the synthetic procedure of hollow prismatic/cylindric iron fluoride: outside-in ripening process (g).

of hollow iron fluorides particles. Template-free methods for generating hollow inorganic micro- and nanostructures have been developed employing some novel mechanisms [8,26–28], including the Ostwald ripening [29], nanoscale Kirkendall effect [30], corrosion-based inside-out evacuation [28]. All of them can be explained by two-step process: self-templated and self-aggregation approaches [31]. For the former it starts from the formation of particles having certain morphology, followed by evacuation to form hollow materials with an inside-out way. For the other, however, it is driven by the oriented attachment mechanism [32], the nearby unstable nanocrystals adjust themselves to close each other and form polyhedra or sphere spontaneously and orderly. In this work, the nanocrystals are formed through the reaction between Fe^{3+} cations and F^- anions during the first stage of reaction. Subsequently, iron fluoride nanocrystals gather together, the completed or incompleted prismatic and cylindric framework take shape at random. With longer reaction times, the primary nanoparticles are close to each other and self-aggregate along the inside wall of sheet prismatic or cylindric framework driving by the oriented attachment mechanism under the low-fluidity conductions. The SEM images show the morphologies of samples where hollow prism and cylinder coexist. When the central cavity is filled up, the fine crystallites began to aggregate on the surface of the prism and cylinder, and generate solid cubes with much larger size. In order to better understand the morphologies feature of iron fluoride changing with time, the formation mechanism of the hollow pentagonal prism, hexagonal prism and cylinder are schematically illustrated in Fig. 2g.

The hollow prismatic and cylindric morphology of F2 can be clearly indicated by the TEM images from Fig. 3a and b. An obvious hole can be observed in the inner of the particle. Besides, it can be recognized from the picture that the particle is composed of many tiny particles about 50 nm. Fig. 3d shows the electron diffraction pattern of F2. Two ring related to (220) and (002) planes of $FeF_3 \cdot 0.33H_2O$. The high-resolution TEM shows well nanocrystalline regions (Fig. 3c) with interplanar distance of about 3.20 Å that is comparable to (220) planes conformed to $FeF_3 \cdot 0.33H_2O$, which is comparable to the SAED image. No obvious $FeF_3 \cdot 3H_2O$ phase has been detected from HRTEM and SAED images, which may be due to the relative small amount of it.

Generally speaking, porous micro/nanometer fluorides cathodes materials have good electrochemical performances [10,17]. Fig. 4a shows the initial discharge/charge profiles of F1, F2 and F4 in the voltage range of 2.0–4.5 V with a current rate of 0.5 C. All samples have only one plateau observed for both the discharge/charge curves, which are related to the lithium ion insertion and extraction process. The electrochemical reaction mechanism of iron fluorides has been previously proposed by our team [19]. In the process of discharge, Li^+ inserts into $FeF_3 \cdot nH_2O$ to form $LiFeF_3 \cdot nH_2O$, causing a slight lattice change of $FeF_3 \cdot nH_2O$, but maintaining the original structure. Contrarily, in the charge process, Li^+ extracts from $LiFeF_3 \cdot nH_2O$ to generate $FeF_3 \cdot nH_2O$.

As described in Fig. 4a and b, F1, F2 and F4 deliver initial discharge specific capacities of 103.0, 106.7 and 62.6 mAh g^{-1}, respectively. After 100 cycles, the discharge capacity of F1, F2 and F4 decrease to 59.5, 63.9 and 46.7 mAh g^{-1}, and their capacity retentions are 57.7%, 60%, 74.6% in turn. F1 and F2 show much higher discharge capacities compare with F4. The specific hollow prismatic morphology has made undeniable contributions since it can provide access to three different contact regions with the electrolyte, namely, the ends, outer and inner surface of the hollow prism and cylinder, thus providing more sites that redox reaction occurs and making intercalation reactions easier. Though F4 delivers lowest charge–discharge capacity, but it has the better capacity retention. It may be speculated that the best crystallinity of F4, as indicated by the XRD pattern in Fig. 1a, resulting in the best capacity retention, but the much larger particle size leads to a lower discharge/charge capacity. Large particle size is adverse to improving the lithium ion diffusion rate, so as to reduce the utilization rate of iron fluorides and make low discharge/charge capacity. They interact with each other makes F4 has the best capacity retention but the lowest discharge/charge capacity among three samples. One more thing to note, from the XRD pattern of Fig. 1a, is the relative content of $FeF_3 \cdot 3H_2O$ and $FeF_3 \cdot 0.33H_2O$ in F4 is much higher than F1 and F2. We hold that, just as we stated in our previous work [19], $FeF_3 \cdot 3H_2O$ shows higher capacity retention comparing with $FeF_3 \cdot 0.33H_2O$. The hydration water plays a major role in determining the electrochemical performances of $FeF_3 \cdot 3H_2O$. On the one hand, the more the hydration water is, the more the hydrogen bond can be formed. This causes stable cell structure leading to higher
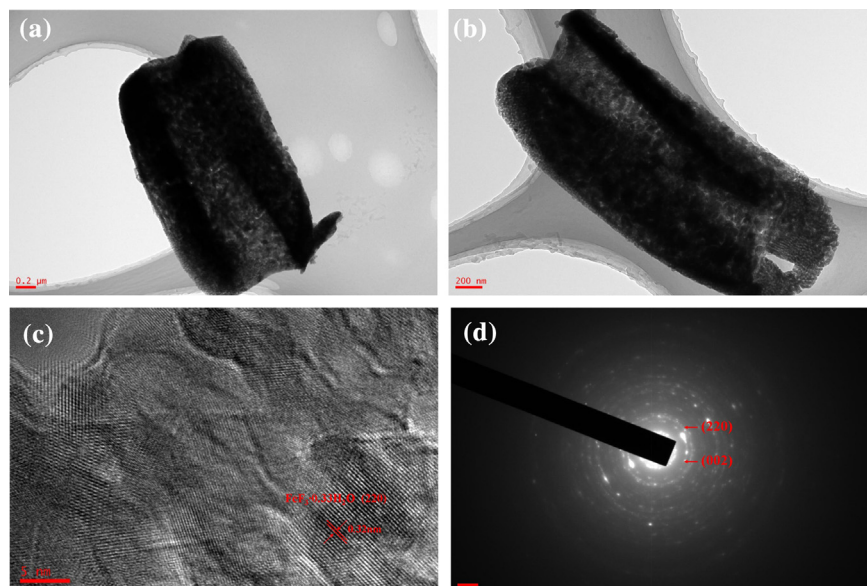

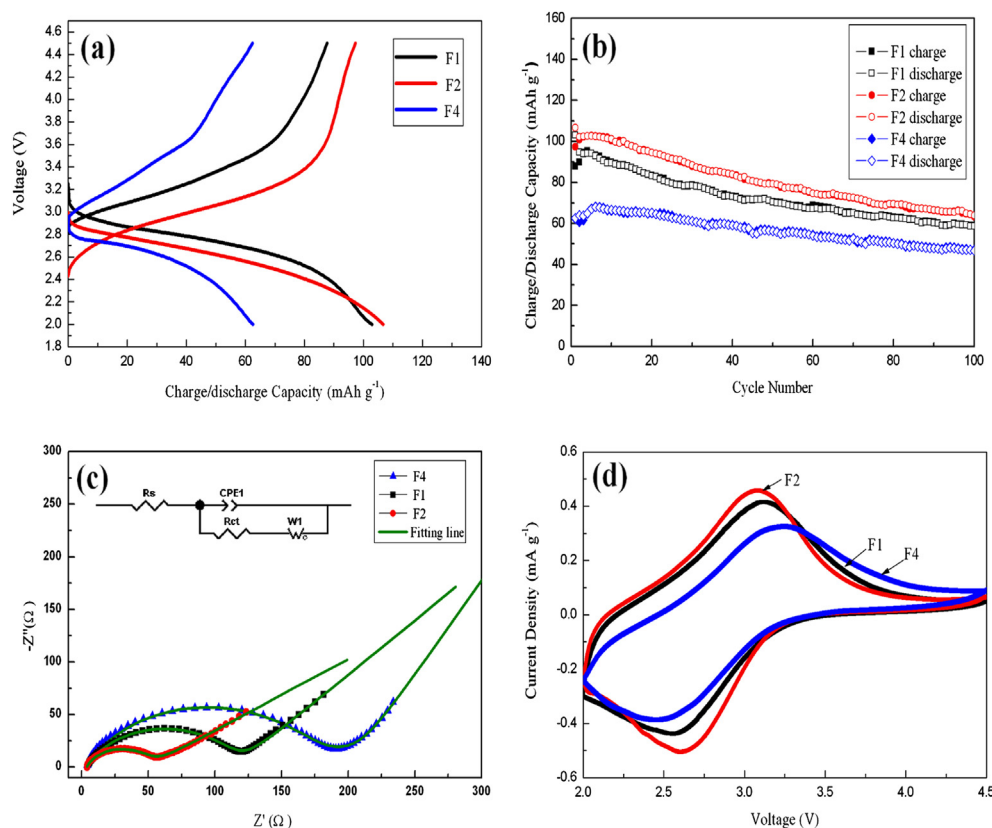**Fig. 3.** TEM (a, b), HRTEM (c) and SAED (d) images of F2.

Fig. 4. Initial discharge and charge profiles (a) cycling stability curves (b) of F1, F2 and F4 at 0.5 C in the voltage of 2.0–4.5 V. Nyquist plots of F1, F2 and F4 after the first cycle (c) (inset: the simplified equivalent circuit model). CV curves of F1, F2 and F4 measured after the first cycle (the scan rate is 1 mV s^{-1}) (d).

capacity retention. On the other hand, the excess of hydration water decreases the quality specific capacity of $FeF_3 \cdot 3H_2O$ remarkably, because the hydration water is not involved in the electrochemical reaction between FeF_3 and Li^+. This results a lower actual discharge/charge capacity. Consequently, F4 shows higher capacity retention, but lower discharge/charge capacity.

The Nyquist plots and CV curves obtained after first cycle are shown in Fig. 4c and d. The Nyquist plots consist of one semicircle in the high frequency region and a sloping line in the low frequency region. The semicircle region is related to the Li^+ charge transfer resistance and the sloping line is associated with the diffusion of Li^+ into the solid matrix. The inset of Fig. 4c shows the simplified equivalent circuit model of the Nyquist plots. The equivalent circuit model is made up of electrolyte resistance (R_s), a constant phase element (CPE) related to the interfacial resistance, and the semicircle is ascribed to the Li^+ charge transfer resistance (R_{ct}) at the solid and liquid phases interface, while the linear portion is designated to Warburg impedance (W_1), which is attributed to the diffusion of Li^+ into the bulk of the electrode materials. The fitted impedance parameters are listed in Table 1. Results indicate that $R_{ct} = 120.12\ \Omega$ and $191.51\ \Omega$ of F1 and F4 were much higher than $R_{ct} = 56.33\Omega$ of F2, all of them obtained in the range of 2.0–4.5 V. The CV curve (Fig. 4d) was measured at the scan rate of 1 mV s^{-1}. These

three electrode materials show a pairs of oxidation–reduction peak, symmetrical redox peaks at 2.58 and 3.11 V, 2.61 and 3.07 V, 2.46 and 3.24 V for F1, F2 and F4, respectively. The corresponding potential interval (ΔE) is found to be 0.53 V, 0.46 V and 0.78 V apart. Apparently, the potential interval of F2 is smaller than F1 and F4, demonstrating small polarization and good reversibility of F2 that checks well with the Nyquist plots. In addition, the peak current density of F2 electrode is also larger than those of F1 and F4 electrode as a consequence of less lithiation/delithiation polarization.

It is seen that, from the SEM images, F1 has a larger surface area than F2 and should have a more active interfacial reaction with the electrolyte solution resulting a higher discharge/charge capacity. However, the discharge/charge capacity of F2 is slightly higher than F1, which may be due to part of the capacity of F1 was consumed to form the initial SEI films leading to a high irreversible capacity, then the SEI films suppressed the further interfacial reactions, given rise to electrochemical resistance of F1 during the process of EIS test (Fig. 4c) and decreased the peak current density of F1 during the process of CV test.

Although F2 shows the best electrochemical activity among the three samples, the actual discharge and charge capacity is much lower than theoretical capacity and the capacity retention is also poor. Wide band gap caused by high ionicity of metal fluorides induces the insulation properties that make the poor electronic conductivity of materials, eventually making low actual specific capacity, fast capacity fading, and prospective poor rate performance. Ball-milling as-prepared iron fluoride with AB powers is a simple and effective method to improve the electrochemical performance of iron fluoride. It can not only reduce material size to short the lithium ion diffusion path and accelerate the dynamics properties, but also make material and AB mixing together

Table 1
R_s and R_{ct} values for F1, F2 and F4 after the first cycle.

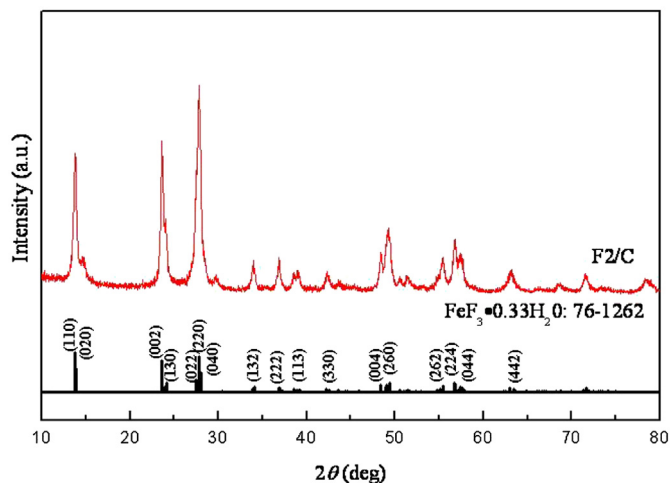| Samples	R_s/Ω	R_{ct}/Ω
F1	4.1461	120.12
F2	3.9529	56.33
F4	4.4597	191.51

Fig. 5. XRD patterns of F2/C.

heterogeneously to form a conductive network and increase the electronic conductivity of materials. Therefore, F2/C has been obtained by ball-milling F2 and AB. Fig. 5 is the XRD patterns of F2/C. The diffraction patterns of F2/C can be indexed to $FeF_3 \cdot 0.33H_2O$ (JCPD card no. 76-1262). There is no carbon signal collected by the reason of the amorphous phase of AB. After ball-milling and heating at 180 °C for 6 h, the $FeF_3 \cdot 3H_2O$ in F2 can be completely transformed to $FeF_3 \cdot 0.33H_2O$ within a short time because the

average particle size of grains gets smaller, inducing lose of hydration water at a much quicker rate. It is important to note that the loss of hydration water in $FeF_3 \cdot 0.33H_2O$ needs much higher temperature [19], so the final product is only $FeF_3 \cdot 0.33H_2O$.

The SEM image of F2/C is shown in Fig. 6a and b. The particle size is obviously reduced after ball-milling with AB. Meanwhile, the tiny particles which have no visible crystal shape agglomerate together to form secondary particles, which are 0.1–1.0 μm. The TEM images of Fig. 6c, d clearly show that F2/C nanocomposites are composed of primary particles with diameters of ~30 nm. Fig. 6e appears a nanocrystalline regions enclosed by an amorphous carbon matrix, indicating $FeF_3 \cdot 0.33H_2O$ and AB evenly mixed together after ball-milling. The SAED image of F2/C presented in Fig. 6f exhibits two ring patterns related to (220) and (002) planes which checks with orthorhombic $FeF_3 \cdot 0.33H_2O$ (JCPD card no. 76-1262).

The discharge and charge profiles of F2/C during the first 5 cycles at 0.1 C in the voltage of 2.0–4.5 V are shown separately in Fig. 7a. The initial discharge capacity of F2/C can achieve 184.7 mAh g^{-1} at 0.1C. In addition, cycling stability curves of F2/C at different rates has also been revealed in Fig. 7b. The initial discharge capacity of F2/C at 0.5 C, 1 C, 2 C and 5 C are 160.2 mAh g^{-1}, 154.4 mAh g^{-1}, 146.3 mAh g^{-1} and 137.5 mAh g^{-1}, respectively. The capacity retentions are as high as 85.0%, 83.9%, 78.1% and 75.7% after 100 cycles. The discharge capacity and capacity retention, especially at the high rate of 5 C (1.185 Ag^{-1}), is comparable to the capacity of 3DOM FeF$_3$/PEDOT composite tested at a current density of 1 Ag^{-1} [17]. The rate capabilities of F2 and F2/C also have been tested from 0.2 C to 5 C (0.2, 0.5, 1, 2 and 5 C) with each rate for 5 cycles (Fig. 7c). F2 and F2/C can retain discharge capacity of 107.6 and 159.6 mAh g^{-1}
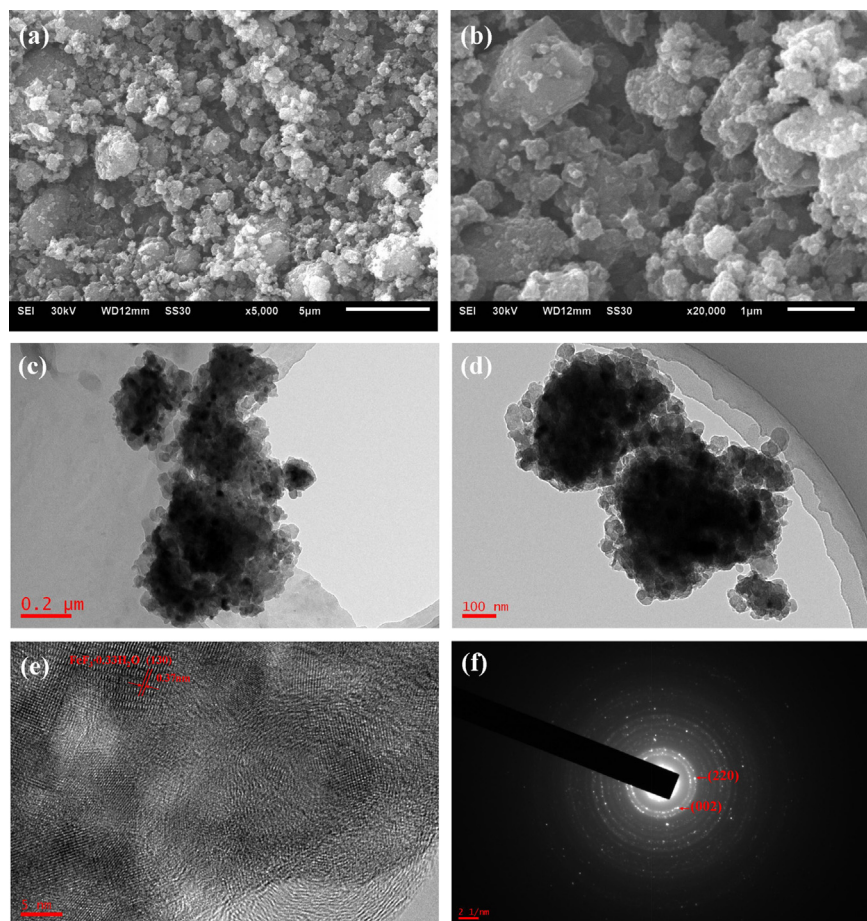

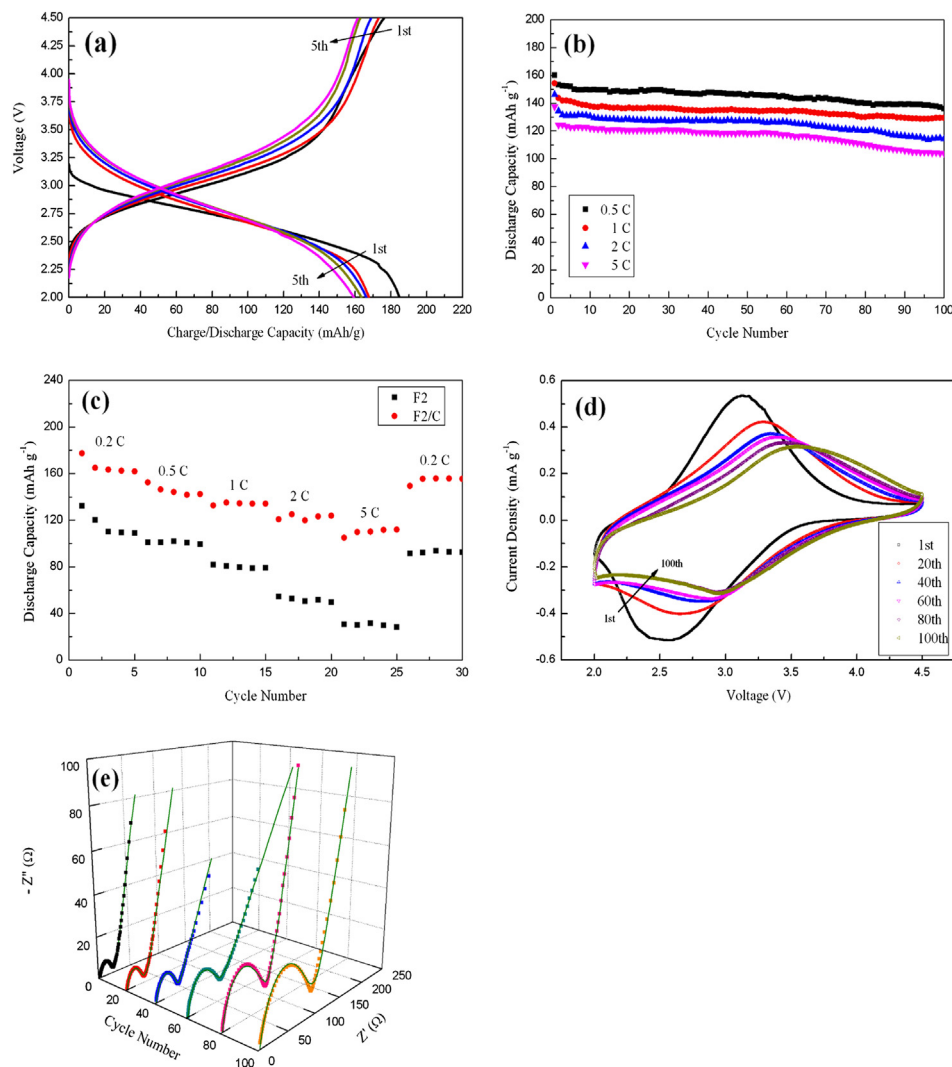**Fig. 6.** SEM (a, b), TEM (c, d), HRTEM (e) and SAED (f) images of F2/C.

Fig. 7. Discharge and charge profiles of F2/C during the first 5 cycles at 0.1 C in the voltage range of 2.0—4.5 V (a). Cycling stability curves of F2/C at 0.5 C, 1 C, 2 C and 5 C in the voltage range of 2.0—4.5 V (b). Three-dimensional Nyquist plots (c) and CV curves (d) for F2/C at different cycles (the scan rate of CV curves is 1 mV s^{-1}).

after 5 cycles at the rate of 0.2 C. Even cycling for 20 cycles at mounting rate, F2/C still can achieve discharge capacity of around 115 mAh g^{-1} at 5 C and around 153 mAh g^{-1} when comes back to 0.2 C. But F2 can only obtain about 43 and 92 mAh g^{-1} at the identical condition. Obviously, the actual capacity, capacity retention and rate capability of materials are improved significantly after ball-milling.

The three-dimensional Nyquist plot of F2/C is presented in Fig. 7e. The fitting process of Nyquist plot is identical with Fig. 4c. It is seen that there is a small R_s difference, but differences are expounded in the Li$^+$ charge transfer resistance (R_{ct}) with the increase of cycles. The R_{ct} values of F2/C electrode measured at 1st, 20th, 40th, 60th, 80th and 100th cycles are 22.36 Ω, 29.26 Ω, 39.63 Ω, 55.49 Ω, 75.49 Ω and 93.47 Ω, respectively. This is consistent with the capacity decay shown in Fig. 7b. To further investigate the electrochemical behaviors of F2/C, the CV curves measured at 1st, 20th, 40th, 60th, 80th and 100th cycles after the EIS test with a scan rate of 1 mV s^{-1} in the voltage of 2.0—4.5 V are shown in Fig. 7d. The CV technique can be used to evaluate the Li$^+$ ions insertion and de-insertion behavior in FeF$_3$·0.33H$_2$O/C nanocomposites. As shown in the first CV curve, a potential peaks at ~2.7 V is observed during the cathodic scan, which indicates the one-step intercalation of the first Li$^+$ in FeF$_3$·0.33H$_2$O/C host and

the phase evolves from FeF$_3$·0.33H$_2$O/C to LiFeF$_3$·0.33H$_2$O/C, the corresponding one anodic peaks at ~3.1 V suggests the good reversibility of the lithium-insertion process, which is comparable with the previous report of our groups [19]. After 20 cycles, the CV curves become largely identical indicating the capacity fading of batteries occurs mainly in the first 20 cycles, particularly in the first 2 cycles. The results are well consistent with the discharge/charge curves in Fig. 7b, where a mainly capacity loss happens between the first and second cycle.

The galvanostatic intermittent titration technique (GITT) has been widely used to determine the lithium ion diffusion coefficient of electrode, and is considered to be a reliable and accurate method [33—37]. The lithium ion diffusion coefficient can be calculated by using the following equation deduced by Weppner and Huggins [33]

$$D_{Li} = \frac{4}{\pi} \left(I_o \frac{V_m}{SFz_i} \right)^2 \left(\frac{dE/dx}{dE/dt^{1/2}} \right)^2 \quad \left(t \ll L^2/D_{Li} \right) \tag{1}$$

where D_{Li} (cm^2 s^{-1}) is the chemical diffusion coefficient of the mobile specie, I_0 (A) is the applied current, V_m (cm^3 mol^{-1}) is the molar volume of the active materials, S (cm^2) is the total contact area between the electrolyte and electrodes, F (96485 C/mol) is the
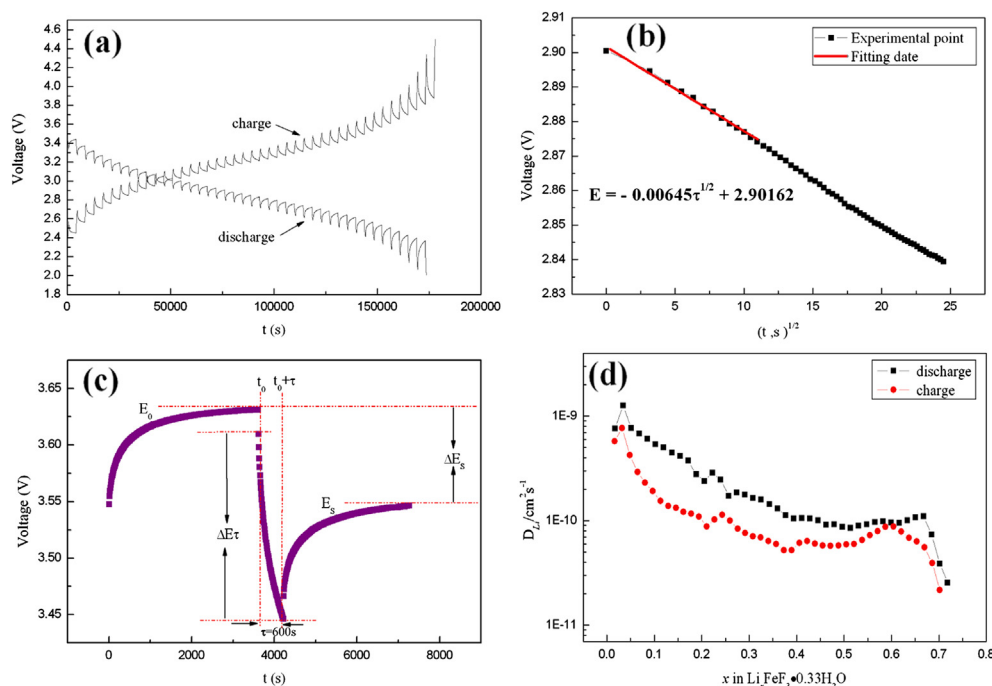
Fig. 8. The discharge/charge GITT curves of F2/C electrode as a function of time in the potential range of 2.0–4.5 V (a). Linear behavior of the transient voltage changes (E) vs ($t^{1/2}$) during a single titration process for F2/C (b). E vs t profile of F2/C electrode for a single GITT during discharge process at 3.55 V with schematic representation of different profile parameters (c). The calculated D_{Li} from the GITT data for F2/C as a function of x (Li insertion number) during discharge process and charge process (d).

Faraday constant, Z_i is the number of charge transfer, and L (cm) is the diffusion length.

To achieve steady-state voltage, an interval of 10 min at a small current flux of 0.1 C ($\sim$23.7 mAh g^{-1}) and a long time interval of 60 min have been combined with the GITT test. Fig. 8a displays the first discharge/charge GITT curves of F2/C electrode as a function of time in the potential range of 2.0–4.5 V. The voltage change has a good linearity with the square root of interruption time during a single titration process (Fig. 8b). It is almost a liner with the scope of 10–100 s, the slope of the liner is used to calculated lithium ion diffusion coefficient. A single step of GITT at 3.55 V during the discharge process is illustrated in Fig. 8c with schematic labeling of different parameters. The lithium ions diffusion coefficient derived according to the Equation (1) are showing in Fig. 8d. It is easy to know from the profiles that in the process of discharge (Li$^+$ insertion), the D_{Li} of F2/C is in the range from 2.55 $\times$ 10^{-11} to 1.26 $\times$ 10^{-9} cm^2 s^{-1}, and in the process of charge (Li$^+$ extraction), the D_{Li} values of F2/C is 2.17 $\times$ 10^{-11} to 1.00 $\times$ 10^{-10} cm^2 s^{-1}, which is consistent with that of FeF$_3\cdot$0.33H$_2$O/C synthesized by liquid phase method [19] and is higher by nearly three order of magnitude than that of D_{Li} for FeF$_3\cdot$0.33H$_2$O (with an upper limit of $\sim$10^{-14} cm^2 s^{-1} at the voltage range of 1.6–4.5 V obtained from PITT) calculated by Li et al. [25].

4. Conclusions

In summary, iron fluoride with mixed crystal structure has been synthesized by a time-dependent solvothermal method. The electrochemical testing results show that the product obtained by solvothermal reacting for 2 h has the best electrochemical properties and unique hollow prismatic/cylindric structure. It delivers the reversible capacity of 106.7 mAh g^{-1} at the rate of 0.5 C in the voltage range of 2.0–4.5 V, which can be attributed to its specific hollow morphology that offers more sites facilitating the insertion and extraction of Li$^+$, and higher crystallinity that implies an unhindered Li$^+$ diffusion in the lattice and the consequent low polarization and high capacity retention. An outside-in ripening mechanism has been used to explain the evolution of hollow prismatic/cylindric iron fluoride. After ball-milling with 15 wt% AB and heat-treatment, the FeF$_3\cdot$0.33H$_2$O/C nanocomposites have been formed and show improved electrochemical properties. FeF$_3\cdot$0.33H$_2$O/C nanocomposites can achieve initial discharge capacity of 160.2 mAh g^{-1} at 0.5C and 137.5 mAh g^{-1} at 5 C, and capacity retentions are as high as 85.0% and 75.6% after 100 cycles at 0.5 C and 5 C, respectively.

References

[1] H. Li, G. Richter, J. Maier, Adv. Mater. 15 (2003) 736.
[2] K. Mizushima, P.C. Jones, P.J. Wiseman, J.B. Goodenough, Mater. Res. Bull. 15 (1980) 783.
[3] T. Li, L. Li, Y. Cao, X. Ai, H. Yang, J. Phys. Chem. 114 (2010) 3190.
[4] H. Arai, S. Okada, Y. Sakurai, J. Yamaki, J. Power Sources 68 (1997) 716.
[5] J. Maier, Nat. Mater. 4 (2005) 805.
[6] a) A.S. Arico, P.G. Bruce, B. Scrosati, J.M. Tarascon, W. Van Schalkwijk, Nat. Mater. 4 (2005) 366;
b) P.G. Bruce, B. Scrosati, J.M. Tarascon, Angew. Chem. Int. Ed. 47 (2008) 2930.
[7] H.G. Yang, H.C. Zeng, Angew. Chem. 116 (2004) 6056.
[8] X.W. Lou, Y. Wang, C.L. Yuan, J.Y. Lee, L.A. Archer, Adv. Mater. 18 (2006) 2325.
[9] C. Li, L. Gu, S. Tsukimoto, P.A. van Aken, J. Maier, Adv. Mater. 22 (2010) 3650.
[10] Q. Chu, Z. Xing, J. Tian, X. Ren, A. Asiri, A. Al-Youbi, K. Alamry, X. Sun, J. Power Sources 236 (2013) 188.
[11] L. Liu, M. Zhou, L.h. Yi, H.P. Guo, J.L. Tan, H.B. Shu, X.K. Yang, Z.H. Yang, X.Y. Wang, J. Mater. Chem. 22 (2012) 17539.
[12] L. Liu, M. Zhou, X.Y. Wang, Z.H. Yang, F.H. Tian, X.Y. Wang, Mater. Sci. 47 (2012) 1819.

[13] C. Li, L. Gu, J. Tong, J. Maier, Nano 5 (2011) 2930.
[14] C. Li, C. Yin, L. Gu, R.E. Dinnebier, X. Mu, Peter A. van Aken, J. Maier, J. Am. Chem. Soc. 135 (2013) 11425.
[15] B. Li, D.W. Rooney, N. Zhang, K. Sun, Appl. Mater. Interfaces 5 (2013) 5057.
[16] Q. Chu, Z. Xing, X. Ren, A. Asiri, A. Al-Youbi, K. Alamry, X. Sun, Electrochim. Acta 111 (2013) 80.
[17] D.L. Ma, Z.Y. Cao, H.G. Wang, X.L. Huang, L.M. Wang, X.B. Zhang, Energy Environ. Sci. 5 (2012) 8538.
[18] F. Badway, F. Cosandey, N. Pereira, G.G. Amatucci, J. Electrochem. Soc. 150 (2003) A1318.
[19] L. Liu, H.P. Guo, M. Zhou, Q.L. Wei, et al., J. Power Sources 238 (2013) 501.
[20] Z. Bai, L. Yang, J. Zhang, L. Li, J. Lv, C. Hu, J. Zhou, Catal. Commun. 11 (2010) 919.
[21] J.S. Xu, Y.J. Zhu, CrystEngComm 14 (2012) 2630.
[22] M.K. Devaraju, I. Honma, Adv. Energy Mater. 2 (2012) 284.
[23] H.T. Huang, C.A. Vincent, P.G. Bruce, J. Electrochem. Soc. 146 (1999) 3649.
[24] A.M. Kannan, A. Manthiram, Electrochem. Solid-State Lett. 5 (2002) A167.
[25] C.L. Li, L. Gu, J. Tong, S. Tsukimoto, J. Maier, Adv. Funct. Mater. 21 (2011) 1391.
[26] H.G. Yang, H.C. Zeng, Angew. Chem. Int. Ed. 43 (2004) 5930.
[27] C.H. Lu, L.M. Qi, J.H. Yang, X.Y. Wang, D.Y. Zhang, J.L. Xie, J.M. Ma, Adv. Mater. 17 (2005) 2562.
[28] Y.J. Xiong, B. Wiley, J.Y. Chen, Z.Y. Li, Y.D. Yin, Y.N. Xia, Angew. Chem. Int. Ed. 44 (2005) 7913.
[29] H.G. Yang, H.C. Zeng, J. Phys. Chem. B 108 (2004) 3492.
[30] Y. Yin, R.M. Rioux, C.K. Erdonmez, S. Hughes, G.A. Somorjai, A.P. Alivisatos, Science 304 (2004) 711.
[31] X.W. Lou, L.A. Archer, Z.C. Yang, Adv. Mater. 20 (2008) 3987.
[32] R.L. Penn, J.F. Banfield, Science 281 (1998) 969.
[33] W. Weppner, R.A. Huggins, J. Electrochem. Soc. 124 (1977) 1569.
[34] Y.M. Choi, S.l. Pyun, Solid State Ionics 109 (1998) 1593.
[35] K.M. Shaju, G.V. Subba Rao, B.V.R. Chowdari, J. Mater. Chem. 13 (2003) 106.
[36] N. Ding, J. Xu, Y.X. Yao, G. Wegner, X. Fang, C.H. Chen, I. Lieberwirth, Solid State Ionics 180 (2009) 222.
[37] J. Liu, X. Sun, Y. Li, X. Wang, Y. Gao, K. Wu, N. Wu, B. Wu, J. Power Sources 245 (2013) 371.